Journal of
Materials Chemistry A

ROYAL SOCIETY
OF CHEMISTRY

PAPER

View Article Online
View Journal | View Issue

Cite this: *J. Mater. Chem. A*, 2024, **12**, 30821

Controlling CO_2 flux in a CO_2-permeable membrane with a H_2O driving force†

Jacqueline A. Penn, Wenting Hu, Ian S. Metcalfe and Greg A. Mutch *

Received 19th July 2024
Accepted 5th October 2024

DOI: 10.1039/d4ta05021e

rsc.li/materials-a

Gas separation membranes hold significant promise for carbon capture and storage (CCS) as they offer high modularity in combination with technical simplicity. It is routinely expected that a difference in the partial pressure of CO_2 (*i.e.*, a CO_2 driving force) across a CO_2-permeable membrane dictates CO_2 flux. Here, however, we show that in a molten-salt membrane fabricated using molten hydroxides, a H_2O driving force in the opposite direction to CO_2 permeation exerts control. We demonstrate this by using the opposing H_2O driving force to operate the membrane in ways that challenge the conventional understanding of CO_2-permeable membranes. For example, increasing the CO_2 flux whilst decreasing the CO_2 driving force. Throughout, we employ a model membrane support to facilitate recovery (and subsequent characterisation) of the molten salt, showing that membranes fabricated using molten hydroxides transform into majority molten carbonate membranes during CO_2 separation. The carbonate : hydroxide ratio is shown to be a function of time, temperature, and gas-phase composition, and high carbonate : hydroxide ratios are correlated with high CO_2 fluxes. Overall, our work demonstrates that molten-salt membranes evolve, and that a H_2O driving force can be used to control CO_2 flux.

1. Introduction

To limit global warming to less than 1.5 °C above pre-industrial levels by 2100, global CO_2 emissions must reach net-zero by 2050. Carbon capture and storage (CCS) is expected to play a critical role in enabling the transition to net-zero.[1] CCS is an attractive option as it can often be deployed without significant process changes, and because it is currently a lower-cost option than many electrification approaches for emission-intensive industries (*e.g.*, cement, iron, steel, refineries, chemicals *etc.*).[2] In addition, it can offer the potential for negative emissions in certain configurations, *i.e.*, in direct air capture,[3] and bioenergy with CCS processes.[4]

There are clear opportunities for membranes in CCS processes, particularly in situations where there are high concentrations of CO_2 in the feed gas (*e.g.*, cement, iron, steel, refineries, chemicals *etc.*), where lower capture rates are tolerable, and at smaller scales. For example, with a feed gas containing 10% CO_2, the energy requirement for a two-stage polymeric membrane process with a capture rate of 60% and >99% CO_2 product is the same as an amine-based solvent process with a capture rate of 90% and >99% CO_2 product. However, if the feed gas contains 30% CO_2, the membrane process requires less than half the energy of the solvent process.[5] Similarly, a comparative techno-economic analysis of post-combustion CO_2 capture (12% CO_2 feed gas; 96% CO_2 product) using a modern amine solvent, solid adsorbent, and a polymeric membrane found that the adsorbent and membrane processes are more cost-competitive with the solvent process when low capture rates are tolerable and at small scales (<100 t CO_2 per day).[6]

Whilst various polymeric membrane materials and process configurations have been investigated for carbon capture, few have made it beyond pilot-plant scale (TRL 5–6).[1,7] Inorganic membranes have been investigated for carbon capture even less, due largely to disadvantages (relative to polymeric membranes) in terms of processability, brittleness, and cost. Nonetheless, at the lab scale (TRL 3–4), they appear to offer good chemical and thermal stability, and in certain configurations, very high CO_2 perm-selectivity (a key performance metric for application in CCS). For example, supported molten-salt membranes (porous inorganic support, infiltrated with a molten salt), have been shown to provide exceptionally high CO_2 perm-selectivity when they are fabricated using molten carbonates (CO_2 permeability of 10^{-12} to 10^{-10} mol m^{-1} s^{-1} Pa^{-1} and CO_2/N_2 selectivity up to 1000).[8] For comparison, state-of-the-art polymeric membranes (TRL 3–4) offer CO_2 permeability one order of magnitude lower (10^{-13} mol m^{-1} s^{-1} Pa^{-1}) and CO_2/N_2 selectivity several orders of magnitude lower (10),[9] whilst for post-combustion CCS in general, CO_2 permeability on the order of 10^{-13}–10^{-12} mol m^{-1} s^{-1} Pa^{-1} in combination with

---

Materials, Concepts & Reaction Engineering (MatCoRE) Group, School of Engineering, Newcastle University, Newcastle upon Tyne, NE1 7RU, UK. E-mail: greg.mutch@newcastle.ac.uk

† Electronic supplementary information (ESI) available. See DOI: **https://doi.org/10.1039/d4ta05021e**

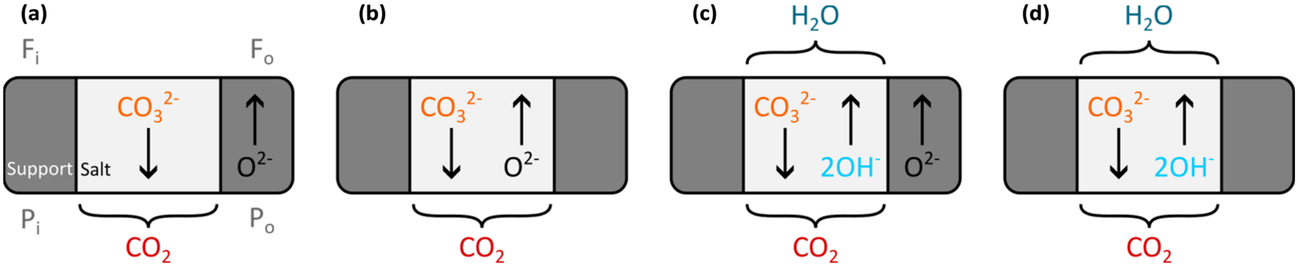

Fig. 1 Proposed mechanisms of counter-diffusion of ionic species in supported molten-salt membranes. (a) Molten carbonate salt with an oxide-ion conducting support and (b) an inert support. (c) Molten carbonates in the presence of a H_2O-containing sweep gas, or molten hydroxides, with an oxide-ion conducting support and (d) an inert support. In (a)–(d), a CO_2-containing feed gas is supplied to the top surface of the membrane, and in (c) and (d), a H_2O-containing sweep gas is supplied to the bottom surface of the membrane. Permeation of CO_2 would therefore occur from top to bottom, and H_2O from bottom to top, as shown here with curved brackets. In (a), F_i and F_o indicate the CO_2 feed-side chamber inlet and outlet respectively, and P_i and P_o indicate the CO_2 permeate-side chamber inlet and outlet respectively. The sweep gas is introduced at P_i. Note that this labelling, as well as "Support" and "Salt", is applicable for (a)–(d).

CO_2/N_2 selectivity of 50–100 is required.[10] Thus, supported molten-salt membranes appear to offer sector-leading CO_2 perm-selectivity, at or beyond the level required for application.

The wide range of observed CO_2 perm-selectivity in supported molten-salt membranes is due, at least in part, to the use of a very wide array of solid support materials and membrane geometries. Support materials have included nominally inert ceramics (*e.g.*, Al_2O_3),[11–13] oxide-ion conducting ceramics (*e.g.*, doped CeO_2),[11,14] mixed electron and oxide-ion conducting ceramics (*e.g.*, $La_{0.6}Sr_{0.4}Co_{0.8}Fe_{0.2}O_{3-\delta}$),[15,16] and metals (*e.g.*, Ag).[17–19] Support geometries have included pellets,[11,12,14–19] hollow fibres,[13,20] and tubes.[19,21–23] As pore volume and tortuosity is expected to impact CO_2 flux,[24–26] these are introduced and/or controlled using a variety of methods, most often by partial sintering of ceramic powders,[11,12,14–17,19] but also by electrochemical dealloying,[18] phase inversion,[13] and tape-casting and freeze-drying.[27] To produce pores with very low tortuosity, advanced manufacturing techniques have also been employed, including laser drilling,[19,23] and laser-directed solidification.[28]

Such a wide array of chemical and physical properties can make detailed comparisons of membrane performance and permeation mechanism difficult, particularly in the absence of thorough characterisation, which is often the case. Nonetheless, various permeation mechanisms relying on the counter-diffusion of ionic species have been proposed to explain experimental observations (Fig. 1). For example, in the case of oxide-ion conducting supports, the counter-diffusion of oxide ions in the solid support, and carbonate ions in the molten carbonates is proposed (Fig. 1a).[29] Due to the lower ionic conductivity of solid supports compared to molten carbonates, increasing the solid fraction of the membrane can lead to higher CO_2 fluxes.[29]‡ In the case of inert solid supports, as there is no route for the transport of ionic species in the solid, CO_2 permeation is expected to be facilitated by the molten carbonate alone. Low CO_2 fluxes observed for membranes with inert supports have been justified based on the low concentration of oxide ions in molten carbonates, compared to the majority ions (*i.e.*, alkali metals and carbonate) (Fig. 1b).

The composition of molten carbonates has also been discussed in the context of H_2O-containing sweep gases. For example, in CeO_2,[14] $BaZr_{0.8}Y_{0.2}O_{3-\delta}$,[30] and $Sc_{0.1}Ce_{0.01}Zr_{0.89}O_{1.95}$,[31] supported molten-salt membranes, CO_2 flux increases of 30 to 300% were observed for H_2O-containing sweep gases, compared to 'dry' sweep gases.§ It was suggested that hydroxide ions in the molten carbonate, formed *via* reaction with H_2O, contributed to an increased flux. In only one study to date, the molten carbonates normally used during membrane fabrication were substituted with molten hydroxides (we note here that this membrane was tested with a H_2O-containing sweep gas also, and employed a CeO_2 support).[32] With H_2O-containing sweep gases, it is proposed that counter-diffusion of hydroxide and carbonate ions occurs in the molten salt, in addition to the counter-diffusion of oxide ions in the solid support and carbonate ions in the molten salt (Fig. 1c), leading to high CO_2 flux.

In the case of the molten-salt membrane fabricated using molten hydroxides, the authors made the interesting suggestion that the molten-salt composition changes in response to the partial pressure of CO_2 in the feed gas. For example, a surprising increase in CO_2 permeability observed with a decrease in the feed-gas CO_2 partial pressure was attributed to the lower CO_2 partial pressure leading to the molten salt having a lower carbonate : hydroxide ratio (and therefore a higher overall ionic conductivity, as molten hydroxides have a higher ionic conductivity than molten carbonates).[32] This suggestion that the composition of molten salts may change in response to gas phase conditions is particularly interesting as it suggests that the starting composition of a molten-salt membrane may be relatively unimportant. A deeper understanding of membrane performance therefore requires detailed characterisation of the molten salt as a function of operating conditions.

---

‡ Assuming due consideration is given to percolation of the molten salt at the highest solid support fractions and noting that the condition of maximum ambipolar diffusion will be different at different temperatures, and for different support materials.

§ Apostrophes around dry (*i.e.*, 'dry') denotes that the precise H_2O concentration in the sweep gases were not measured/provided.

A final complication for all the work on supported molten-salt membranes is in understanding the exact nature of the CO_2 flux-driving force relationship. Recent work studied the partial pressure dependence of CO_2 flux in a membrane with an oxide-ion conducting support and molten carbonates under 'dry' conditions (Fig. 1a).§ This was achieved by varying the porosity of the support and therefore solid fraction of the membrane.[26] Whilst the authors noted that CO_2 flux generally increased with CO_2 partial pressure in the feed gas, there were important differences noted. When CO_2 flux was controlled by carbonate-ion conduction in the molten salt (low porosity support/high solid fraction), CO_2 flux showed a logarithmic dependence on CO_2 partial pressure (eqn (1)). When CO_2 flux was controlled by oxide-ion conduction in the solid phase (high porosity support/low solid fraction), a power-law dependence on CO_2 partial pressure was shown (eqn (2)),

$$J_{CO_2} \propto \ln\left(\frac{p'_{CO_2}}{p''_{CO_2}}\right) \tag{1}$$

$$J_{CO_2} \propto \left(p'^{n}_{CO_2} - p''^{n}_{CO_2}\right) \tag{2}$$

where J_{CO_2} is the flux of CO_2, and p'_{CO_2} and p''_{CO_2} are the partial pressures of CO_2 at the feed and permeate sides of the membrane, respectively. Thus, one might expect CO_2 flux in molten-salt membranes fabricated using molten carbonates and inert supports to follow a logarithmic relationship (as there is no route for transport in the solid support, and therefore carbonate-ion conduction must control flux). Indeed, this relationship was observed in our recent work under dry sweep-gas conditions (<100 ppm H_2O).[33] However, with H_2O present in the sweep gas, the CO_2 driving force no longer had a strong effect on CO_2 flux, and instead, a H_2O driving force appeared to exert control (eqn (3)),

$$J_{CO_2} \propto \ln\left(\frac{p''_{H_2O}}{p'_{H_2O}}\right) \tag{3}$$

where J_{CO_2} is the flux of CO_2, and p'_{H_2O} and p''_{H_2O} are the partial pressures of H_2O at the feed and permeate sides of the membrane, respectively. Note that as H_2O was fed to the permeate side of the membrane (in the sweep gas), the driving force for H_2O (and therefore, H_2O permeation) was in the opposite direction to the CO_2 driving force (and therefore, CO_2 permeation). In the same work we showed that carbonate-like ions in molten carbonates can act as a carrier for both CO_2 and H_2O, with their transport occurring in opposite directions.[33] The mechanism involved several energetically-viable transport routes, with complex, inter-connected equilibria and different carrier forms, so the reader is referred to that work for further detail. Overall, however, H_2O at the CO_2 permeate-side, gas-membrane interface drove the release of CO_2 from that interface and CO_2 at the CO_2 feed-side, gas-membrane interface drove the release of H_2O at that interface, from a shared carbonate-like carrier.

Based on our recent work and the discussion above, we were motivated to investigate the potential for changes to molten-salt composition with operating conditions *e.g.*, time, temperature, and gas-phase composition, and to understand the role of the H_2O driving force on CO_2 flux in membranes fabricated using molten hydroxides. To limit permeation to the molten salt alone, and to attempt to simplify mechanism (Fig. 1d), we prepared a model, inert support with pores of very low tortuosity (laser-drilled alumina) (Fig. 2), which was infiltrated with molten hydroxides. A series of permeation experiments and corresponding characterisations of recovered molten salts were performed to understand the role of H_2O in H_2O-containing feed and sweep gases on CO_2 flux, and on molten-salt composition. Importantly, we monitored the H_2O concentration at both sides of the membrane continuously (whilst also monitoring the permeate-side outlet for CO_2). This is unusual, as it has been common practice to only measure the permeate-side outlet (to measure CO_2 flux) in experiments with supported molten-salt membranes. This allowed us to experimentally demonstrate the counter-permeation of CO_2 and H_2O in a membrane fabricated using molten hydroxides for the first time. Moreover, there was a very clear influence of both the

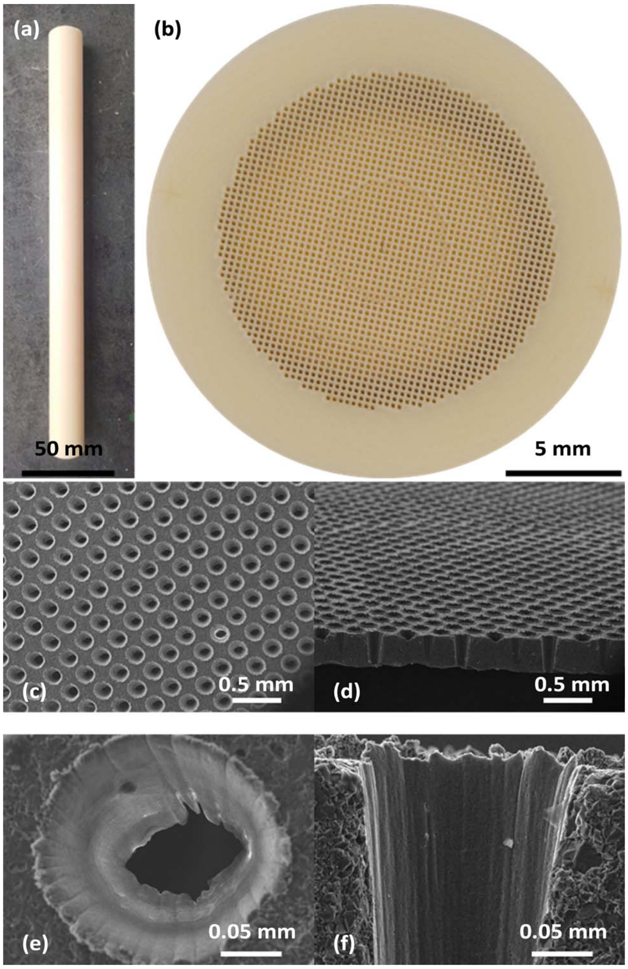

Fig. 2 Molten-salt membrane support. (a) Dense alumina tube with one closed end. (b) Laser-drilled holes on the closed end, and (c–f) SEM images of the laser-drilled holes in top-down and cross-section views.

molten-salt composition (carbonate : hydroxide ratio) and particularly the H_2O driving force (from CO_2 permeate side to CO_2 feed side) on CO_2 flux (from CO_2 feed side to CO_2 permeate side).

2. Experimental

2.1 Materials

Lithium hydroxide (powder, reagent grade, ≥98%), sodium hydroxide (powder, reagent grade, 97%), potassium hydroxide (powder, for synthesis), hydrochloric acid solution (0.1 mol l^{-1} reagent grade) and phenolphthalein solution (0.5% w/w in ethanol : water (1 : 1)) were purchased from Sigma-Aldrich. Lithium carbonate (powder, 99%), sodium carbonate (powder, 98%) and potassium carbonate (granular, ≥99%) were purchased from Alfa Aesar. Bromocresol green (sodium salt, 0.04% w/v aqueous solution) was purchased from Thermo Fisher Scientific. Fully dense alumina tubes with one closed end were purchased from Precision Ceramics (length 235 ± 1.6 mm, outer diameter (OD) 19.05 mm, inner diameter (ID) 17.78 mm, OD/ID $\pm$ 0.635 mm, and closed-end thickness 0.46 mm) (Fig. 2a). The closed ends of the tubes were laser drilled by Laser Micromachining Ltd to form an array of ~2000 truncated conical holes (~150 μm entrance, ~50 μm exit) on a square pitch of ~250 μm (Fig. 2b–f). A perfluoropolyether based, chemically inert, high-temperature vacuum grease (PFPE 501) was purchased from Apiezon. All gases were supplied by BOC.

2.2 Membrane preparation, membrane reactor and flow system

A mixture containing 43.5 mol% lithium hydroxide, 31.5 mol% sodium hydroxide, and 25 mol% potassium hydroxide was prepared, and thoroughly mixed in a Fluxana MUK mixer, inside a nitrogen glove box (to avoid deliquescence and limit reaction with atmospheric CO_2). The composition of the hydroxide mixture was chosen as upon full conversion to carbonate, the carbonate ternary eutectic would form. The hydroxide mixture was stored in the glove box, with portions weighed out and removed periodically to make pellets for permeation experiments. These pellets were prepared by pressing the amount of hydroxide mixture required to fill the volume of the laser-drilled holes (upon melting) at 3 tons in an Atlas Power T25 hydraulic press, with the pellets having the diameter required to cover the laser-drilled area.

The laser-drilled, closed-end alumina tube was housed in a custom-made membrane reactor,[19,23,33] with gas inlets/outlets and a thermocouple port positioned near the closed end of the alumina tube (Fig. S1a†). The tube (outer diameter ~19 mm) was placed inside the stainless-steel base of the membrane reactor (inner diameter ~20 mm), and vacuum grease was applied around this connection to form the seal. The pellet of hydroxide mixture was placed on the laser-drilled, closed end of the tube. A quartz cover was then sealed to the base of the membrane reactor using a rubber O-ring under compression. This arrangement creates two chambers: a CO_2 feed-side chamber inside the alumina tube, and a CO_2 permeate-side chamber between the alumina tube and quartz cover, with both chambers having a gas inlet and outlet (Fig. S1a†). Hereafter, these are frequently referred to simply as feed-side chamber and permeate-side chamber. Based upon the residence time distribution response for both chambers (Fig. S2†), the membrane was considered to be exposed to the outlet conditions of each chamber.

The constructed membrane reactor was located within a vertical split-tube furnace (Vecstar) and connected to an automated flow system containing mass flow controllers (Brooks) and 4-way electronic valves (VICI), which allowed for the delivery of feed- and sweep-gas streams (Fig. S1b and c†). All flow rates, for all experiments and gas mixtures, were set to 50 ml min^{-1} (NTP), by measuring the appropriate gas-stream outlet using an electronic flow meter (GFM Pro, Thermo Scientific).

The flow system permitted the independent humidification of the feed- and sweep-gas streams, due to the presence of two in-line, water-filled permeation tubes. These consist of two water-filled reservoirs, separated from the gas streams by two water-permeable membranes, contained within two furnaces. The quantity of water transferred across the water-permeable membranes, and therefore the resulting H_2O concentration in the gas streams, was controlled by varying the temperature of the furnaces (Fig. S3†).

2.3 Permeation experiments and measurement of CO_2 and H_2O flux

To melt the hydroxide mixture, and infiltrate the laser-drilled holes, the membrane reactor was heated to the experimental temperature at 2 °C min^{-1}. During heating, ~1% H_2O in Ar was supplied to both the feed-side and permeate-side chamber inlets, to limit decomposition of the hydroxide mixture.[34] At the experimental temperature, the feed-side chamber inlet was switched to a CO_2 in N_2 mixture, whilst the permeate-side chamber inlet remained as Ar (throughout the experimental campaign, the feed- and permeate-side gas streams were humidified to different extents). The presence of different inert gases in the feed- and permeate-side streams (N_2 and Ar) permitted the detection of transmembrane leaks. Experiments were stopped if N_2 was detected significantly above background levels in the permeate-side outlet, or if N_2 levels were seen to be increasing (see below).

The CO_2 and/or H_2O mole fraction in the feed- and permeate-side outlet streams were monitored by two, in-line infrared analysers (LI-COR, LI-850 CO_2/H_2O). The mole fraction of N_2 in the permeate-side outlet stream was also monitored by a quadrupole mass spectrometer (Hiden, QGA), connected to the outlet of the corresponding infrared analyser. The infrared analysers and mass spectrometer were calibrated to account for systematic error, and any air ingress into the membrane reactor, flow system, or analytical equipment. This was performed by flowing Ar (99.999%, total impurities ≤10 ppm maximum, typical impurity concentrations: 3 ppm H_2O, 6 ppm N_2, 2 ppm O_2) through the flow system, membrane reactor, infrared analysers, and mass spectrometer to obtain a background. The background measured before an experiment confirmed the absence of significant leaks into the experimental apparatus, whilst the background measured after an experiment was subtracted from the collected experimental data. Typically, the background levels were ~200 ppm of N_2 and ~10 ppm of CO_2. Gases of certificated mole fraction (369 ppm CO_2 in Ar, 400 ppm N_2 in Ar, and 903 ppm H_2O in Ar) were used to calibrate the infrared analysers and mass spectrometer. Instrumental drift in the mass spectrometer was also accounted for by normalising CO_2, H_2O, and N_2 signals against Ar (majority species).

The mole fraction of CO_2 and/or H_2O in the permeate-side outlet was converted to flux (mol s^{-1} m^{-2}) using eqn (4),

$$J_i = \frac{y_i Q_G}{60 \times 22400} \times \frac{1}{A} \tag{4}$$

where J_i is the flux of i (here, CO_2 or H_2O), y_i is the mole fraction of i in the gas phase at the outlet, Q_G is the volumetric flow rate at the outlet (ml min^{-1}), and A is the permeate-side area of the membrane (m^{-2}). As two supports were used throughout the experimental campaign, the permeate-side areas used were 0.35 and 0.47×10^{-5} m^{-2}, based on the specific number of laser-drilled holes in each.

2.4 Membrane characterisation

Following permeation experiments, the molten salt component of the membrane was recovered by sonicating the laser-drilled, closed-end of the cooled membrane in ~60 ml of deionised water for 30 minutes at 35 °C. Subsequently, 8 ml samples were titrated against 0.1 mol l^{-1} HCl, using the two indicators separately (phenolphthalein and bromocresol green). Phenolphthalein indicates (ν_1) upon complete conversion of CO_3^{2-} to HCO_3^-, and bromocresol green indicates (ν_2) upon complete conversion of CO_3^{2-} to H_2CO_3. The titration was performed in triplicate, with the mean volume of HCl consumed used in calculations; ($\nu_2 - \nu_1$) for CO_3^{2-}, and $(2(\nu_1) - \nu_2)$ for OH^-.[32,35,36] The reliability of the titration was tested both for accuracy compared to known mixtures of hydroxides and carbonates, and for any effect that cooling procedures (rate and atmosphere) had on composition. We note here that the titration was shown to accurately identify the composition of seven different known mixtures, and that the largest difference between actual and measured composition was <4% (Table S1†). Moreover, the rate of cooling and cooling atmosphere did not appear to have a significant effect (Table S2†), and therefore all membranes were cooled in dry Ar (Ar with ≤3 ppm H_2O) at 5 °C min^{-1}.

Samples of the laser-drilled, closed-end alumina tubes, both prior to permeation experiments and following several, extended permeation experiments lasting a total of ~800 h (~500 h at 400–700 °C, and ~300 h of heating/cooling), were prepared by cutting with a diamond saw (Top Tech Precision, CL40). A first cut removed the closed end of the tubes, to create a pellet shape containing the laser-drilled holes. A second cut split the pellet shape in two, creating semi-circular pieces and revealing the cross section. The prepared samples were rinsed with deionised water, and sonicated in deionised water for 30 minutes at 35 °C. For SEM imaging and EDX analysis, the semi-circular samples were carbon coated (EMScope TB500) before analysis with a JSM-IT510 InTouchScope™ Scanning Electron Microscope with integrated EDX. Images and EDX spectra were taken under high vacuum with secondary electron detection using an accelerator voltage of 20 kV and a working distance of 10 mm. Images and EDX spectra were collected from various sample orientations to access different surfaces, and within the laser-drilled holes (*i.e.*, the cross-section view). Samples without carbon coating were analysed by Raman spectroscopy (Horiba LabRAM HR Evolution) using a 455 mW, 532 nm Nd:YAG laser (Laser Quantum), a non-dispersive filter to reduce the power at the sample to between ~50 and 100% of the laser power, a 600 g mm^{-1} grating and a 20× objective (Olympus LMPLFLN20X). Each Raman spectrum was obtained as 10–15 accumulations of 10–15 s acquisitions.

3. Results and discussion

3.1 CO_2 flux with an alternating wet and dry sweep gas

A hydroxide-infiltrated membrane was heated to 600 °C with ~1% H_2O in Ar supplied to both the feed- and permeate-side chamber inlets, before the feed-side chamber inlet was switched to 50% CO_2 in N_2 (the permeate-side chamber inlet remained as ~1% H_2O in Ar). CO_2 flux was measured, before cycling between a dry (Ar with ≤3 ppm H_2O) and wet (~1% H_2O in Ar) sweep gas (Fig. 3). Despite there being a CO_2 partial pressure difference across the membrane (*i.e.*, a CO_2 driving force), initially there was no significant CO_2 flux. At ~2.5 h, CO_2 flux 'breakthrough' occurred, before the CO_2 flux reached ~2.5 $\times 10^{-4}$ mol s^{-1} m^{-2}. Upon switching to the dry sweep gas at 3 h, there was a decrease in CO_2 flux, reaching ~1×10^{-5} mol s^{-1} m^{-2} at 6 h. Note that hereafter, we frequently refer to fluxes on the order of 10^{-4} mol s^{-1} m^{-2} as 'high', and fluxes on the order of 10^{-5} mol s^{-1} m^{-2} as 'low', for simplicity, and due to the order-of-magnitude difference.

Further cycling between the wet and dry sweep gas resulted in a similar response from the membrane, *i.e.*, abrupt, order-of-magnitude changes between high and low CO_2 flux, and a clear

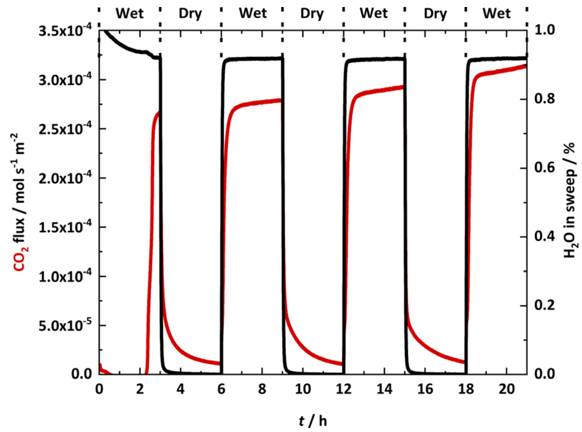

Fig. 3 CO_2 flux with an alternating wet and dry sweep gas. Feed-side chamber inlet: 50% CO_2 in N_2. Permeate-side chamber inlet: dry (Ar with ≤3 ppm H_2O) and wet (~1% H_2O in Ar). T = 600 °C.

link between the presence of H_2O in the sweep gas and high CO_2 flux. It was also notable that the CO_2 flux in the wet cycles increased across the cycles. First, the high flux achieved at the end of the previous wet cycle was recovered quickly before the flux continued to increase slowly. As the conditions (temperature, CO_2 concentration in the feed gas, H_2O concentration in the sweep gas *etc.*) of the wet cycles remained constant, this implied that the membrane composition might be changing in time. We note here that characterisation of the membrane support (SEM-EDX and Raman as described in Section 2.4) showed that even after ~800 h (>1 month) of membrane operation, there were no significant changes to the physical properties of the membrane support (Fig. S4†), and that there were only minor changes to the support chemistry (*e.g.*, limited formation of $LiAlO_2$) (Table S3 and Fig. S5†). This suggested that the order-of-magnitude changes in CO_2 flux occurring on much shorter timescales (between wet and dry cycles of 3 h) were more likely arising due to the presence of H_2O in the sweep gas, and that changes occurring on even shorter timescales (breakthrough and increasing flux within wet cycles) may be due to an evolving molten-salt composition.

3.2 CO_2 flux as a function of time and H_2O concentration in the feed and sweep gases

Considering the potential for changes in the molten salt with time, and a clear link between CO_2 flux and the presence of H_2O in the sweep gas (Fig. 3), two series of experiments were conducted. In the first series, CO_2 flux and molten-salt composition (titrations with the recovered salt as described in Section 2.4), were measured as a function of time with fixed feed- and sweep-gas compositions (Fig. 4a). In the second series, the H_2O concentration in the feed and sweep gas was varied, with the CO_2 flux and membrane composition measured after a fixed amount of time (Fig. 4b). All experiments were conducted at 600 °C. Thus, the first series investigated the effect of time in the presence of a H_2O-containing sweep gas, and the second series investigated the effect of H_2O concentration in the H_2O-containing sweep gas (and in one case, the feed gas). To attempt to avoid any influence of membrane 'history', all experiments were carried out separately, *i.e.*, following recovery of the salt from the membrane support by washing (as described in Section 2.4), the membrane support was re-infiltrated with fresh molten hydroxides and tested at a different condition (recalling that no significant changes were noted in the membrane support following >1 month of operation). Examples of the full experimental traces (*i.e.*, mole fractions of CO_2, N_2 and H_2O on the permeate side) from the permeation experiments and titration data are provided in Fig. S6 and Table S4† for the first series (Fig. 4a), and in Fig. S7 and Table S5† for the second series (Fig. 4b).

In the first series (effect of time), hydroxide-infiltrated membranes were heated to 600 °C with ~1% H_2O in Ar supplied to both the feed- and permeate-side chamber inlets, before the feed-side chamber inlet was switched to 50% CO_2 in N_2 and the permeate-side chamber inlet was switched to ~0.5% H_2O in Ar. After 0, 5, 10, 20, 30, 40, and 50 h of operation following the gas switches (in separate experiments), CO_2 flux was recorded (points in Fig. 4a) and triplicate titrations were carried out to characterise the recovered molten salt (bars in Fig. 4a).

First, it was noted again that there was a breakthrough period in all the experiments, after which CO_2 flux increased significantly in the absence of any other changes (Fig. S6†). The breakthrough period was of approximately the same duration in

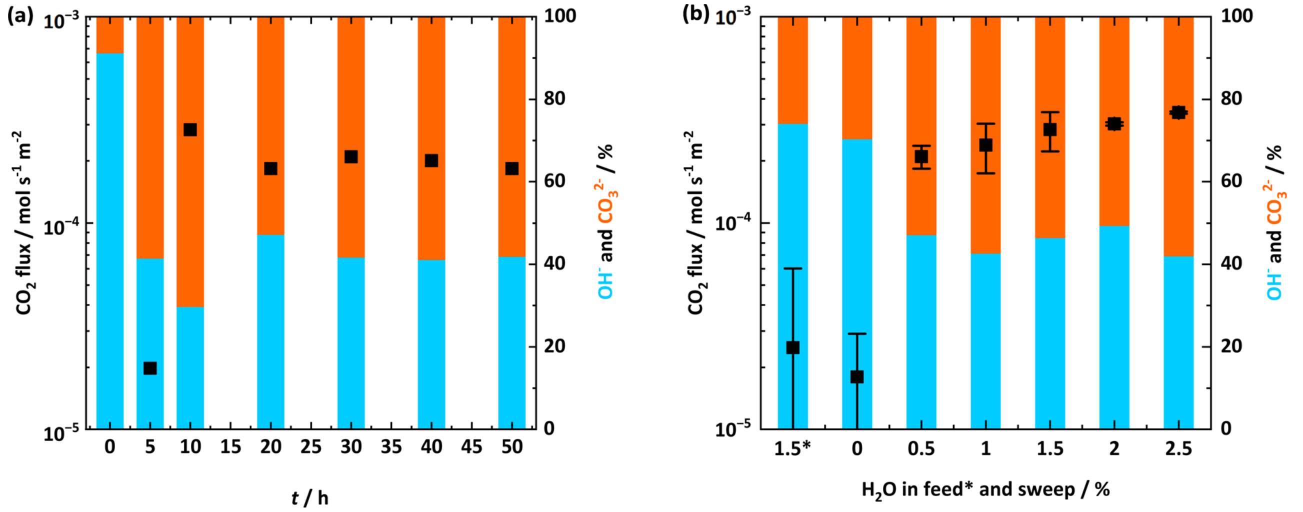

Fig. 4 CO_2 flux as a function of time and H_2O concentration in feed and sweep gases. In both (a) and (b) points are CO_2 flux, and coloured bars are triplicate titrations of recovered salts. (a) CO_2 flux and titrations of recovered salts after separate experiments lasting for 0, 5, 10, 20, 30, 40, and 50 h. Feed-side chamber inlet: 50% CO_2 in N_2. Permeate-side chamber inlet: ~0.5% H_2O in Ar. $T = 600$ °C. (b) Mean CO_2 flux with standard deviation ($n = 2–4$) and titrations of recovered salts after separate 20 h experiments with different H_2O concentrations in feed (marked with an *) and sweep gas. Feed-side chamber inlet: 50% CO_2 in N_2 (with 1.5% H_2O for *). Permeate-side chamber inlet: dry (Ar with ≤3 ppm H_2O) for * and 0, and ~0.5, 1, 1.5, 2, and 2.5% H_2O in Ar. $T = 600$ °C. Full experimental traces and data for (a) are provided in Fig. S6, and Table S4†. Example experimental traces for (b) are provided in Fig. S7,† and the repeats used to calculate mean and error bars in (b) are provided in Table S5†.

each separate experiment (~5 h). For this reason, the CO_2 flux reported at 5 h in Fig. 4a is low as it is taken from transient data where CO_2 breakthrough is beginning (Fig. S6a†). Nonetheless, this makes for an interesting comparison, as it is notable that after 5 h, the molten-salt composition was relatively stable at ~60% carbonate : ~40% hydroxide (bars), whilst the CO_2 flux (points) was also high (on the order of 10^{-4} mol s^{-1} m^{-2}). Although there are small differences in the CO_2 flux and composition, we must recall here that these results are taken from separate permeation experiments and their corresponding triplicate titrations, and that we are discussing an order-of-magnitude difference in CO_2 flux before and after breakthrough. We also note here that the 0 h membrane (heated to 600 °C with ~1% H_2O in Ar supplied to both the feed- and permeate-side chamber inlets but cooled in dry Ar without being exposed to the 50% CO_2 in N_2 feed gas) had a recovered salt composition of ~10% carbonate : ~90% hydroxide. This is expected, as despite handling and preparing the hydroxide mixture under an inert gas in a glove box, atmospheric CO_2 will react with the hydroxide pellet during the amount of time required to prepare the membrane (between the hydroxides leaving the glove box and the permeation experiment starting), and during the time required to recover the hydroxides from the membrane afterwards (between the membrane being removed from the reactor and the titration being performed).

In the second series (effect of H_2O concentration), hydroxide-infiltrated membranes were heated to 600 °C with ~1% H_2O in Ar supplied to both the feed- and permeate-side chamber inlets, before the feed-side chamber inlet was switched to 50% CO_2 in N_2, as above. However, here the permeate-side chamber inlet was switched to ~0 (dry, Ar with ≤3 ppm H_2O), 0.5, 1.0, 1.5, 2.0, and 2.5% H_2O in Ar in separate experiments. Additionally, in a further separate experiment, ~1.5% H_2O was added to the 50% CO_2 in N_2 feed gas (with the sweep gas being dry Ar). As discussed in more detail below, the permeation experiments were repeated several times to assess experimental uncertainty (Table S5†). Following ~20 h at each condition, CO_2 flux was recorded (points in Fig. 4b are the mean and error bars are standard deviation from the repeated permeation experiments), and corresponding triplicate titrations were carried out (bars in Fig. 4b), before the membrane was reinfiltrated and tested at the next condition. Before discussing the results, we note again that there was a breakthrough period in every experiment of ~5 h, and that 20 h was chosen based on the results in Fig. 4a (*i.e.*, no significant change in molten-salt composition or CO_2 flux was expected).

First, it was apparent that under a dry sweep gas (Ar with ≤3 ppm H_2O), CO_2 flux was low and on the same order of magnitude (10^{-5} mol s^{-1} m^{-2}) as in the dry cycles of Fig. 3. Second, whilst adding ~1.5% H_2O to the feed gas did not result in any significant increase in CO_2 flux, there was also no deleterious effect on CO_2 flux. This is important, as there are significant costs associated with drying feed gases to combat deleterious effects in other classes of membranes, *e.g.*, polymeric membranes.[6] When ~0.5% H_2O was added to the sweep gas, however, the CO_2 flux increased, again by an order of magnitude to 10^{-4} mol s^{-1} m^{-2}. Moreover, the CO_2 flux appeared to increase further as the H_2O concentration in the sweep gas increased (Fig. 4b).

Considering that all the discussion so far has related to order-of-magnitude arguments, here we assessed experimental uncertainty by repeating CO_2 flux measurements for each condition up to four times (Table S5†). This repetition was to check whether any differences in CO_2 flux were beyond experimental uncertainty. Indeed, the CO_2 flux did increase with increasing H_2O concentration in the sweep gas. Interestingly, the molten-salt composition showed a corresponding trend (bars in Fig. 4b). Under dry sweep-gas conditions and with H_2O in the feed gas (when CO_2 flux was low, on the order of 10^{-5} mol s^{-1} m^{-2}), the recovered salts were ~25% carbonate : ~75% hydroxide. Conversely, under wet sweep-gas conditions (when CO_2 flux was high, on the order of 10^{-4} mol s^{-1} m^{-2}), the recovered salts were ~60% carbonate : ~40% hydroxide. We note that this composition is the same as that following breakthrough (at and after 5 h) in Fig. 4a.

Here it is important to highlight that the CO_2 flux in Fig. 4b is increasing as the H_2O driving force in the opposite direction is increasing, as in our recent work with a molten-salt membrane fabricated using molten carbonates we showed that CO_2 flux can depend on the H_2O driving force in the opposite direction (eqn (3)).[33] Considering the results in Fig. 4b, it seemed reasonable to suspect that the H_2O driving force may be influencing CO_2 flux here also, but this time in a membrane fabricated using molten hydroxides. To test this hypothesis, the measurement of both permeate-side and feed-side outlet composition is required to see if CO_2 and H_2O are counter-permeating, and to test the extent of the influence that the H_2O driving force (from CO_2 permeate-side to CO_2 feed-side) has over CO_2 flux (from CO_2 feed-side to CO_2 permeate-side).

3.3 Measuring the counter-permeation of CO_2 and H_2O and evidencing the role of the H_2O driving force on CO_2 flux

To investigate the counter-permeation of CO_2 and H_2O, a hydroxide-infiltrated membrane was heated to 600 °C with ~1% H_2O in Ar supplied to both the feed- and permeate-side chamber inlets, before the feed-side chamber inlet was switched to 50% CO_2 in N_2 and the permeate-side chamber inlet was switched to ~0 (dry, Ar with ≤3 ppm H_2O), 1, and 1.5% H_2O in Ar, in a single, continuous experiment (Fig. 5). The CO_2 flux was calculated from the permeate-side outlet composition, and the H_2O flux was calculated from the feed-side outlet composition. There was clear evidence for the counter-permeation of H_2O and CO_2, *i.e.*, with increases in the concentration of H_2O in the sweep gas, the fluxes of H_2O and CO_2 (in opposite directions) both increased. Moreover, it appeared that the magnitude of the CO_2 and H_2O fluxes were similar, suggesting that their permeation was linked (we note that this was also the case in our prior work with a membrane fabricated using molten carbonates).[33]

With the understanding that CO_2 and H_2O counter-permeate, and that their permeation may be linked, it is therefore important to consider the role of the H_2O driving force on CO_2 flux. Thus, in a final series of permeation experiments, the CO_2 driving

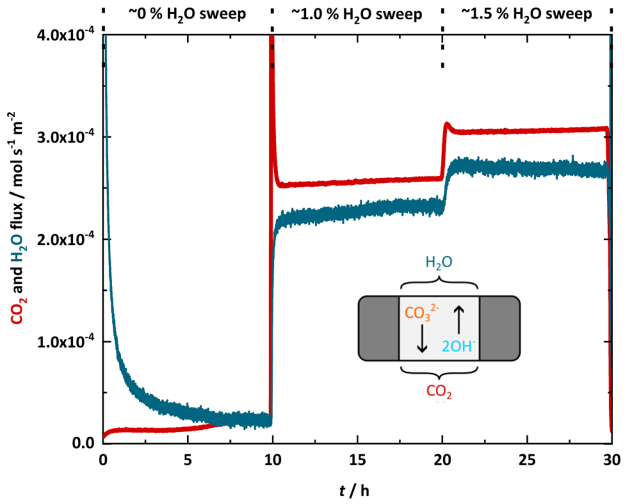

Fig. 5 Counter-permeation of CO_2 and H_2O. CO_2 flux (measured at the permeate-side outlet) and H_2O flux (measured at the feed-side outlet), *i.e.*, in opposite directions (inset schematic). Feed-side chamber inlet: 50% CO_2 in N_2. Permeate-side chamber inlet: ~0 (dry Ar with ≤3 ppm H_2O), 1, and 1.5% H_2O in Ar. $T = 600$ °C.

force was increased whilst the H_2O driving force in the opposite direction was held constant, and conversely, the CO_2 driving force was held constant whilst the H_2O driving force in the opposite direction was increased. This was achieved by heating hydroxide-infiltrated membranes to 600 °C with ~1% H_2O in Ar supplied to both the feed- and permeate-side chamber inlets, before the feed-gas chamber inlet was switched to 1.5, 10 or 50% CO_2 in N_2, whilst the permeate-side chamber inlet was switched to ~1, 1.5, or 2.0% H_2O in Ar (Fig. 6). The results shown in Fig. 6 are from three separate experiments using the three different feed gases (1.5, 10, and 50% CO_2 in N_2). During the experiments with the 1.5 and 10% CO_2 in N_2 feed gases, the permeate-side chamber inlet was increased from ~1, to 1.5 and 2.0% H_2O in Ar after 10 h at each condition. The CO_2 flux (points) is an average of 5 h of stable CO_2 flux, 5 h after the change in the permeate-side chamber inlet condition. During this 5 h period, the CO_2 flux was measured every 5 s, and the maximum variation in CO_2 flux was 6%.

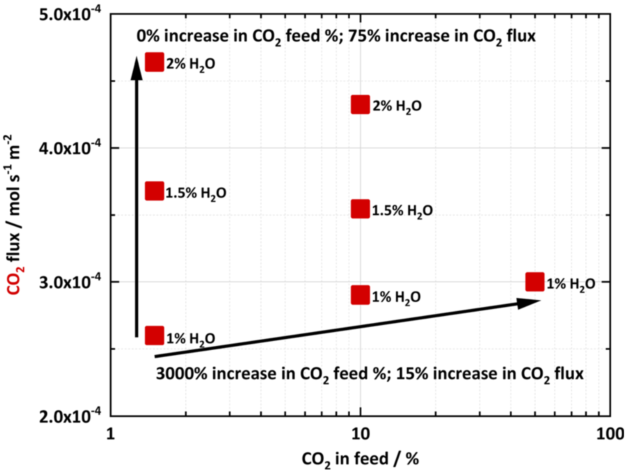

Fig. 6 The role of the H_2O driving force on CO_2 flux. CO_2 flux measured at the permeate-side outlet. Feed-side chamber inlet: 1.5, 10, or 50% CO_2 in N_2. Permeate-side chamber inlet: ~1, 1.5, or 2.0% H_2O in Ar. $T = 600$ °C. Arrows highlight ~3000% increase in linear CO_2 driving force and corresponding ~15% increase in CO_2 flux, and 0% increase in linear CO_2 driving force and corresponding ~75% increase in CO_2 flux.

With a ~3000% increase in feed-gas CO_2 concentration (from 1.5 to 50%), CO_2 flux increased by ~15% (which based on the results in Fig. 4b is within our experimental uncertainty). Whilst initially the lack of a significant increase in CO_2 flux with a significant increase in the CO_2 driving force might be surprising, this is due to the assumption that CO_2 flux should be linked only to the CO_2 driving force. If instead the H_2O driving force is exerting control over the CO_2 flux, this result can be explained based on the ~1% H_2O supplied for both feed-gas conditions, *i.e.*, the CO_2 driving force may not have a strong influence in the presence of H_2O in the sweep gas.

We note that these results in Fig. 6 are consistent with the only previous article that studied a membrane fabricated using molten hydroxides.[32] In that work, the authors reported an unusual apparent CO_2 permeability increase as the feed-gas CO_2 concentration was decreased from 50 to 20% CO_2, whilst the sweep gas contained 4.5% H_2O. Based on their method to determine permeability (which assumed eqn (2) with $n = 1$), were the fluxes with the 50 and 20% CO_2 feed gases similar, the apparent permeability would be expected to increase by a factor of ~2.5 (*i.e.*, 50/20), which was indeed the case (from ~6.5 to ~16 × 10^{-11} mol m^{-1} Pa^{-1} s^{-1}).[32] Were we to use the same approach here, we would report a ~30-fold increase in apparent permeability (*i.e.*, 50/1.5), for CO_2 fluxes that are within our experimental uncertainty. Moreover, the authors suggested that the apparent increase in CO_2 permeability with a decrease in CO_2 driving force was likely due to the lower feed-gas CO_2 concentration resulting in a lowering of the carbonate : hydroxide ratio in the membrane during operation.[32] They suggested this as molten hydroxides have a higher ionic conductivity than molten carbonates, however, no direct experimental evidence was provided to support this assertion. Contrasting with this prior suggestion, our results from triplicate titrations carried out following further, separate experiments with 10 and 50% CO_2 feed gases, suggested that there was no significant difference in the carbonate : hydroxide ratio (Table S6†). It is also worth noting that these titrations were performed on salts recovered from permeation experiments with 10 and 50% CO_2 feed gases (and a ~1% H_2O in Ar sweep gas) where the temperature was increased from 500, to 600, and 700 °C. The CO_2 fluxes at 700 °C for both feed gas conditions were the same at ~7 × 10^{-4} mol s^{-1} m^{-2}, the highest reported in our work (Fig. S8†). Interestingly, the carbonate : hydroxide ratio was also the highest reported at ~80% carbonate : ~20% hydroxide (Table S6†). We also wish to highlight here again the results in Fig. 4b, where CO_2 flux increased with an increasing concentration of H_2O in the sweep gas, but the composition of the membrane remained relatively constant at ~60% carbonate : ~40% hydroxide. Thus, overall, it seems likely that a lowering of the carbonate : hydroxide ratio may not explain increases in CO_2 flux, as across several of our experiments, high CO_2 fluxes are correlated with high carbonate : hydroxide ratios. Moreover, although CO_2 permeability can be made to increase with a reduction in the CO_2 feed-gas concentration, this is simply due to the use of a linear CO_2 driving force (assuming eqn (2) with $n = 1$) in the calculation of CO_2 permeability when the CO_2 flux is not changing significantly (due to the influence of the opposing H_2O driving force).

Finally, and to demonstrate very clearly the importance of controlling the opposing H_2O driving force, the H_2O concentration in the sweep gas was increased whilst the feed-gas chamber inlet was held constant at 1.5 or 10% CO_2 in N_2. Despite 1.5% CO_2 being the lowest feed-gas CO_2 concentration employed in our work (and therefore the lowest CO_2 driving force), the CO_2 flux was at the highest level we report at 600 °C (>4.5×10^{-4} mol s^{-1} m^{-2}). This was achieved by increasing the H_2O concentration in the sweep gas from ~1, to 1.5, and 2% (Fig. 6), which increased the opposing H_2O driving force (Fig. 1d). This ~100% increase in the opposing H_2O driving force had a much more significant effect on CO_2 flux (~75% increase) than that of a ~3000% increase in CO_2 driving force, which resulted in a ~15% increase in CO_2 flux. Moreover, the ~75% increase in CO_2 flux is occurring without an increase in CO_2 driving force. Thus, whereas one might expect the CO_2 driving force, not the opposing H_2O driving force, to exert more significant control on CO_2 flux, it appears that both the CO_2 and H_2O driving forces impact CO_2 flux, but that the opposing H_2O driving force has a much more significant effect (compare arrows in Fig. 6).

We note here that our discussion of *e.g.*, a ~100% increase in the opposing H_2O driving force, and a ~3000% increase in CO_2 driving force (both also labelled on Fig. 6) is based on assuming linear driving force models (for simplicity of discussion). However, it is also apparent that none of the previously proposed CO_2 flux-driving force relationships (eqn (1)–(3)), including the linear model (eqn (2) with $n = 1$), can describe the results in Fig. 6 adequately, and that a much more complex relationship exists between the measured CO_2 flux and the partial pressures of the gases present. To develop such relationships, considering the four partial pressures involved (CO_2 on the feed and permeate side, and H_2O on the feed and permeate side), we note that this becomes a very large, multi-dimensional kinetic space to sample.

4. Conclusions

Detailed understanding of promising CO_2-permeable membranes is important for the future CCS sector. In this work, we have carefully interrogated a model molten-salt membrane to understand the role of H_2O on CO_2 flux. Whilst it had been shown previously that CO_2 flux increases when H_2O is introduced to the sweep gas of molten-salt membranes fabricated using molten carbonates and molten hydroxides, prior attempts at explaining this phenomenon invoked arguments based on a higher ionic conductivity of molten hydroxides compared to molten carbonates. Instead, in this work, we have shown that a molten-salt membrane fabricated using molten hydroxides becomes majority molten carbonate (~60%) following breakthrough of CO_2, which then remains majority molten carbonate under conditions that provide high CO_2 fluxes (*i.e.*, with H_2O in the sweep gas). Conversely, the membrane remains majority molten hydroxide (~75%) under conditions that provide low CO_2 fluxes (under a dry sweep gas and when H_2O is present only in the feed gas). Increasing the H_2O concentration in the sweep gas did not appear to modify the molten-salt composition further, but the CO_2 flux did increase further. Thus, both molten-salt composition and H_2O driving force exert control over CO_2 flux in molten-salt membranes fabricated using molten hydroxides.

To demonstrate the importance of the H_2O driving force, several examples were provided where the careful application of the H_2O driving force (in the opposite direction to the CO_2 driving force and CO_2 flux) was used to challenge our routine understanding of CO_2-permeable membranes. This included driving CO_2 flux from 1.5 and 10% CO_2 feed gases to levels higher than that achieved with a 50% CO_2 feed gas. Interestingly, the highest CO_2 fluxes (~7×10^{-4} mol s^{-1} m^{-2} at 700 °C for both the 10 and 50% CO_2 feed gases with a ~1% H_2O in Ar sweep gas) were correlated with the highest carbonate content in the molten salt (~80%).

Overall, our results suggest that the composition of the molten salt in a molten-salt membrane is a function of time, temperature, and gas-phase composition, which is why we have been careful throughout to refer to different molten-salt membranes as being fabricated using a given molten salt. Moreover, controlling the H_2O driving force in the opposite direction to CO_2 permeation is required to exploit the potential of molten-salt membranes, and calculations intended to communicate this performance clearly (*e.g.*, CO_2 permeability) must be considered in this context. For example, calculating a CO_2 permeability using a linear CO_2 driving force may be somewhat meaningless when there is an opposing H_2O driving force, as one can arrive at very different apparent CO_2 permeabilities when the CO_2 flux has not changed (and *vice versa*). For this reason, as is common practice with *e.g.*, temperature and CO_2 feed-gas concentration, measuring and reporting the sweep-gas H_2O concentration alongside CO_2 permeability should now be required.

Data availability

The data presented in this work is available at **https://data.ncl.ac.uk/**, DOI: **https://doi.org/10.25405/data.ncl.26335333**.

Author contributions

JAP (investigation); JAP and WH (formal analysis, validation); JAP and GAM (visualization, writing – original draft, data curation); JAP, ISM and GAM (conceptualization, methodology); JAP, WH, ISM and GAM (writing – review & editing); ISM and GAM (supervision, project administration, funding acquisition, resources).

Conflicts of interest

There are no conflicts to declare.

Acknowledgements

This work was supported by the Engineering & Physical Sciences Research Council [grant numbers EP/V047078/1, EP/W03395X/1, EP/Y034961/1]. ISM acknowledges funding from the Royal Academy of Engineering through a Chair in Emerging Technologies Award entitled "Engineering Chemical Reactor Technologies for a Low-Carbon Energy Future" (Grant CiET1819/2/57). GAM was supported by the Royal Academy of Engineering under the Research Fellowship scheme. The authors are grateful to Dr Ingham of IGIsystems for helpful discussions during the design and operation of the flow system, and to the Electron Microscopy and Analysis Unit, SAgE Analytical, Newcastle University for assistance with the SEM-EDX measurements.

Notes and references

1 M. Bui, C. S. Adjiman, A. Bardow, E. J. Anthony, A. Boston, S. Brown, P. S. Fennell, S. Fuss, A. Galindo, L. A. Hackett, H. J. Herzog, G. Jackson, J. Kemper, S. Krevor, G. C. Maitland, M. Matuszewski, I. S. Metcalfe, C. Petit, G. Puxty, J. Reimer, D. M. Reiner, E. S. Rubin, S. A. Scott, N. Shah, B. Smit, J. P. M. Trusler, P. Webley, J. Wilcox and N. MacDowell, *Energy Environ. Sci.*, 2018, **11**, 1062–1176.

2 D. Danaci, M. Bui, C. Petit and N. Mac Dowell, *Environ. Sci. Technol.*, 2021, **55**, 10619–10632.

3 M. Erans, E. S. Sanz-Pérez, D. P. Hanak, Z. Clulow, D. M. Reiner and G. A. Mutch, *Energy Environ. Sci.*, 2022, **15**, 1360–1405.

4 M. Fajardy and N. Mac Dowell, *Energy Environ. Sci.*, 2017, **10**, 1389–1426.

5 R. W. Baker, B. Freeman, J. Kniep, Y. I. Huang and T. C. Merkel, *Ind. Eng. Chem. Res.*, 2018, **57**, 15963–15970.

6 S. E. Zanco, J.-F. Pérez-Calvo, A. Gasós, B. Cordiano, V. Becattini and M. Mazzotti, *ACS Eng. Au*, 2021, **1**, 50–72.

7 R. Hou, C. Fong, B. D. Freeman, M. R. Hill and Z. Xie, *Sep. Purif. Technol.*, 2022, **300**, 121863.

8 G. A. Mutch, L. Qu, G. Triantafyllou, W. Xing, M. L. Fontaine and I. S. Metcalfe, *J. Mater. Chem. A*, 2019, **7**, 12951–12973.

9 B. Comesana-Gandara, J. Chen, C. G. Bezzu, M. Carta, I. Rose, M.-C. Ferrari, E. Esposito, A. Fuoco, N. B. McKeown and J. C. Jansen, *Energy Environ. Sci.*, 2019, **12**, 2733–2740.

10 T. C. Merkel, H. Lin, X. Wei and R. Baker, *J. Membr. Sci.*, 2010, **359**, 126–139.

11 J. L. Wade, C. Lee, A. C. West and K. S. Lackner, *J. Membr. Sci.*, 2011, **369**, 20–29.

12 M. Kazakli, G. A. Mutch, L. Qu, G. Triantafyllou and I. S. Metcalfe, *J. Membr. Sci.*, 2020, **600**, 117855.

13 M. Kazakli, G. A. Mutch, G. Triantafyllou, A. G. Gil, T. Li, B. Wang, J. J. Bailey, D. J. L. Brett, P. R. Shearing, K. Li and I. Metcalfe, *J. Membr. Sci.*, 2021, **617**, 118640.

14 W. Xing, T. Peters, M. L. Fontaine, A. Evans, P. P. Henriksen, T. Norby and R. Bredesen, *J. Membr. Sci.*, 2015, **482**, 115–119.

15 M. Anderson and Y. S. Lin, *J. Membr. Sci.*, 2010, **357**, 122–129.

16 E. I. Papaioannou, H. Qi and I. S. Metcalfe, *J. Membr. Sci.*, 2015, **485**, 87–93.

17 N. Xu, X. Li, M. A. Franks, H. Zhao and K. Huang, *J. Membr. Sci.*, 2012, **401–402**, 190–194.

18 J. Fang, N. Xu, T. Yang, P. Zhang, J. Tong and K. Huang, *J. Membr. Sci.*, 2017, **523**, 439–445.

19 L. A. McNeil, G. A. Mutch, F. Iacoviello, J. J. Bailey, G. Triantafyllou, D. Neagu, T. S. Miller, E. I. Papaioannou, W. Hu, D. J. L. Brett, P. R. Shearing and I. S. Metcalfe, *Energy Environ. Sci.*, 2020, **13**, 1766–1775.

20 Z. Xu, Q. Zheng, S. Wang, Z. Zhang, Z. Liu, G. Zhang and W. Jin, *J. Membr. Sci.*, 2021, **635**, 119506.

21 X. Dong, J. Ortiz Landeros and Y. S. Lin, *Chem. Commun.*, 2013, **49**, 9654–9656.

22 X. Dong, H.-C. Wu and Y. S. Lin, *J. Membr. Sci.*, 2018, **564**, 73–81.

23 S. Tsochataridou, G. A. Mutch, D. Neagu, E. I. Papaioannou, M. L. Sanjuán, B. Ray, R. I. Merino, V. M. Orera and I. S. Metcalfe, *ACS Appl. Mater. Interfaces*, 2020, **12**, 16436–16441.

24 Z. Rui, M. Anderson, Y. S. Lin and Y. Li, *J. Membr. Sci.*, 2009, **345**, 110–118.

25 J. Ortiz-Landeros, T. Norton and Y. S. Lin, *Chem. Eng. Sci.*, 2013, **104**, 891–898.

26 J. Y. S. Lin and O. Ovalle-Encinia, *J. Membr. Sci. Lett.*, 2023, **3**, 100041.

27 S. G. M. Carvalho, E. N. S. Muccillo, F. C. Fonseca, M. Müller, F. Schulze-Küppers, S. Baumann, W. A. Meulenberg, O. Guillon and R. Muccillo, *J. Membr. Sci.*, 2022, **648**, 120355.

28 L. Grima, G. A. Mutch, P. B. Oliete, W. Bucheli, R. I. Merino, E. I. Papaioannou, J. J. Bailey, M. D. Kok, D. J. L. Brett, P. R. Shearing, I. S. Metcalfe and M. L. Sanjuán, *J. Membr. Sci.*, 2021, **630**, 119057.

29 F. M. B. Marques, S. G. Patrício, E. Muccillo and R. Muccillo, *Electrochim. Acta*, 2016, **210**, 87–95.

30 K. Zhang, S. Sun, N. Xu and K. Huang, *J. Membr. Sci.*, 2022, **650**, 120421.

31 S. Sun, Y. Wen and K. Huang, *ACS Sustainable Chem. Eng.*, 2021, **9**, 5454–5460.

32 M. R. Cerón, L. S. Lai, A. Amiri, M. Monte, S. Katta, J. C. Kelly, M. A. Worsley, M. D. Merrill, S. Kim and P. G. Campbell, *J. Membr. Sci.*, 2018, **567**, 191–198.

33 I. S. Metcalfe, G. A. Mutch, E. I. Papaioannou, S. Tsochataridou, D. Neagu, D. J. L. Brett, F. Iacoviello, T. S. Miller, P. R. Shearing and P. A. Hunt, *Nat. Energy*, 2024, **9**, 1074–1083.

34 T. Terai, H. Mohri and Y. Takahashi, *J. Nucl. Mater.*, 1991, **179–181**, 808–811.

35 E. P. Partridge and W. C. Schroeder, *Ind. Eng. Chem., Anal. Ed.*, 1932, **4**, 271–273.

36 A. A. Benedetti-Pichler, M. Cefola and B. Waldman, *Ind. Eng. Chem., Anal. Ed.*, 1939, **11**, 327–332.